

Accepted Manuscript

Imidazopyridinium cations: A new family of azonia aromatic heterocycles with applications as DNA intercalators

Pedro Bosch, Verónica García, Başak S. Bilen, David Sucunza, Alberto Domingo, Francisco Mendicuti, Juan J. Vaquero



PII: S0143-7208(16)30903-2

DOI: [10.1016/j.dyepig.2016.11.041](https://doi.org/10.1016/j.dyepig.2016.11.041)

Reference: DYPI 5610

To appear in: *Dyes and Pigments*

Received Date: 17 October 2016

Revised Date: 21 November 2016

Accepted Date: 22 November 2016

Please cite this article as: Bosch P, García V, Bilen BS, Sucunza D, Domingo A, Mendicuti F, Vaquero JJ, Imidazopyridinium cations: A new family of azonia aromatic heterocycles with applications as DNA intercalators, *Dyes and Pigments* (2016), doi: 10.1016/j.dyepig.2016.11.041.

This is a PDF file of an unedited manuscript that has been accepted for publication. As a service to our customers we are providing this early version of the manuscript. The manuscript will undergo copyediting, typesetting, and review of the resulting proof before it is published in its final form. Please note that during the production process errors may be discovered which could affect the content, and all legal disclaimers that apply to the journal pertain.

Imidazopyridinium cations: a new family of azonia aromatic heterocycles with applications as DNA intercalators

Pedro Bosch,¹ Verónica García,² Başak S. Bilen,³ David Sucunza,^{1,*} Alberto Domingo,²
Francisco Mendicuti,³ Juan J. Vaquero^{1,*}

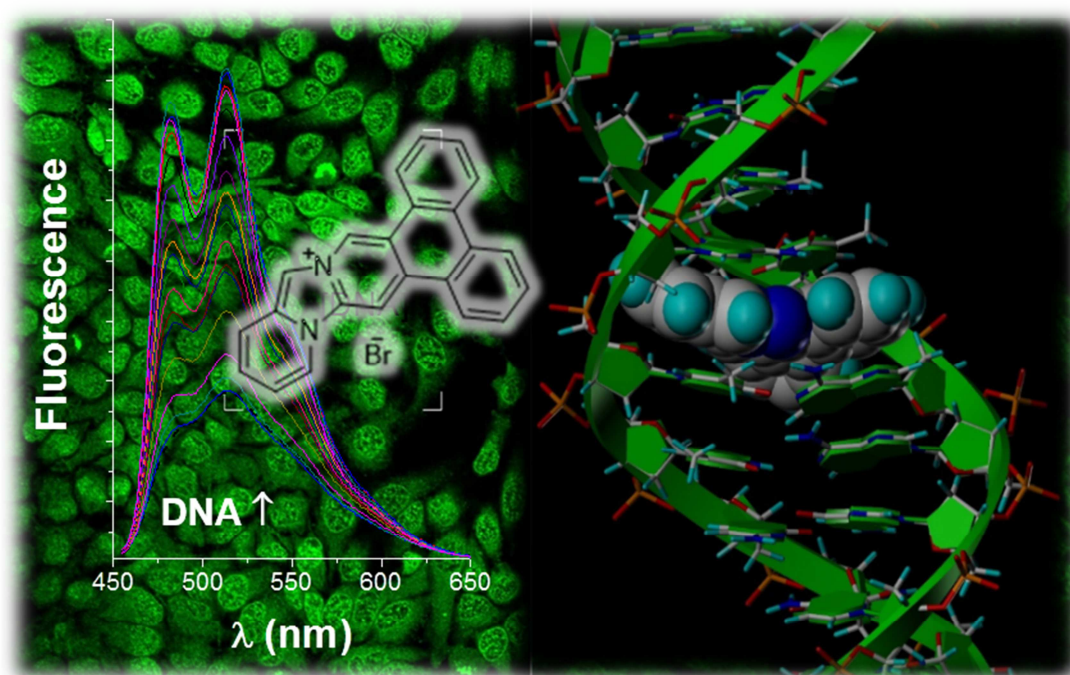
¹*Departamento de Química Inorgánica y Química Orgánica,* ²*Departamento de Biología de Sistemas,* ³*Departamento de Química Analítica, Química Física e Ingeniería Química,*
Universidad de Alcalá, 28871- Alcalá de Henares, Madrid, Spain.

david.sucunza@uah.es, juanjose.vaquero@uah.es

ABSTRACT: Two novel imidazopyridinium cations formed by a hexacyclic azonia aromatic system have been synthesized. Spectrofluorimetric titrations, circular dichroism measurements, theoretical simulations and fluorescence-based thermal denaturation experiments on these materials have shown the interesting fluorescence properties and DNA-binding ability by intercalation, with a marked preference for AT-rich sequences. Compound **2** presents the highest fluorescence quantum yield (0.32 in 5% DMSO/water and 0.46 in MeOH) and affinity for DNA (binding constant of $\sim 4.5 \times 10^5 \text{ M}^{-1}$). Moreover, the potential of these compounds for cell staining has been investigated in living HeLa cells by confocal microscopy imaging. This analysis showed the remarkable capacity of both compounds for uptake and accumulation by living cells.

KEYWORDS: Imidazopyridinium cations, azonia aromatic heterocycles, DNA intercalation, cell staining

GRAPHICAL ABSTRACT:



ACCEPTED MANUSCRIPT

1. Introduction

Polycyclic heteroarenes are usually regarded as representative DNA intercalators, especially if they possess electron-deficient or charged aromatic cores.¹ This class of DNA-binding ligand can affect many biological properties of DNA, including replication and transcription, and they therefore have potential as chemotherapeutic drugs.² The binding of these molecules to DNA is characterized by the insertion of planar aromatic rings between the DNA base pairs, which in turn enables the π -stacking interaction. On the other hand, a positive charge enhances the propensity of a molecule to bind to DNA due to this association results in cation release from the DNA backbone and the solvation of these cations in the aqueous solution contributes to the overall binding energy.³ In most cationic dyes, this positive charge is established by an exocyclic ammonium functionality or by an endocyclic pyridinium moiety. However, cationic dyes with an endocyclic quaternary bridgehead nitrogen atom represent a promising platform for the design of DNA-binding ligands.⁴

Coralyne is probably the most widely studied example of this latter kind of polyaromatic azonia cation.⁵ Interest in this synthetic alkaloid analog is due to several significant properties associated with its structure, a penta-substituted dibenzo[*a,g*]quinolizinium system, such as cytotoxicity,⁶ intercalative DNA binding,⁷ potent topoisomerase inhibition,⁸ and applications as a fluorescent probe.⁹ This interest has also led to a significant amount of research on the synthesis and study of coralyne analogs and other related azonia aromatic heterocycles that contain a quinolizinium system as the core heterocycle.¹⁰ In this sense, recent significant contributions by Ihmels and col.,¹¹ Becq and col.,¹² and us¹³ have shown that these cations are a representative family of DNA intercalators with fluorescence properties, with some examples used as fluorescent probes.¹⁴

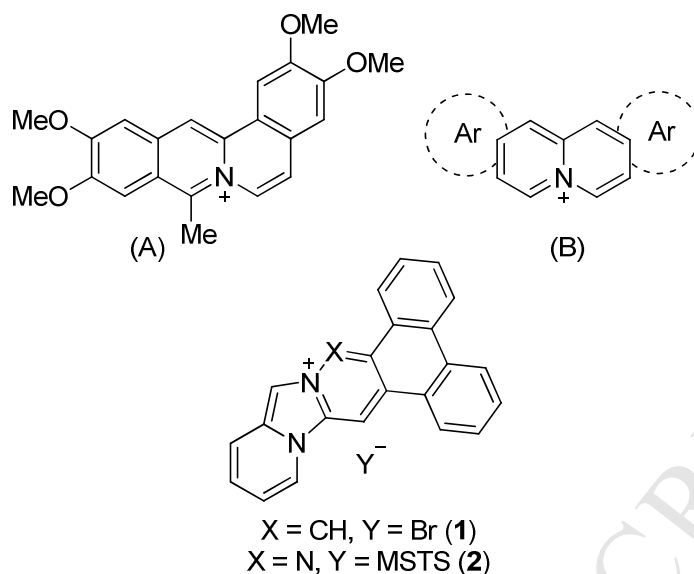


Figure 1. Structure of coralyne (A), the general structure of quinolizinium-based azonia cations (B) and imidazopyridinium cations **1** and **2**.

Less attention has been paid to other polyaromatic azonia cations that contain a quaternary bridgehead nitrogen atom in the core heterocycle. For instance, imidazopyridinium derivatives constitute an interesting family of cations whose DNA-binding capacity has hardly been studied.¹⁵ As part of our research in this area,¹⁶ we report here the synthesis of two novel imidazopyridinium derivatives **1** and **2**, which have shown relatively high fluorescence quantum yields and DNA-binding ability by intercalation.

Both compounds are formed by a hexacyclic azonia system. Although in the literature a fused bicyclic system is considered to be the minimum size for this type of compound,¹⁷ results obtained previously by our group show that a minimum number of four fused rings is needed to produce an interaction with DNA in these systems with a quaternary bridgehead nitrogen atom.^{16,18} This observation can be explained by an enhanced interaction between DNA base pairs and the π system, so the extent of the π system is a key parameter that determines the strength of the DNA association. The systems differ in the presence of an additional nitrogen in the latter compound, a change that should provide further information about the effect of replacing a methylene group next to the quaternary nitrogen atom of quinolizinium with another

nitrogen. Similar binding constants have usually been found in compounds with this structural difference.⁷

Moreover, the capacity for cell staining of compound **2** was investigated in living HeLa cells by confocal microscopy imaging. The results of this analysis show a remarkable capacity of this cation for live-cell uptake and staining of interphase nuclei and metaphase chromosomes.

2. Methods, materials and protocols

2.1. Synthetic procedures

2.1.1. General information. Reagents of the highest commercial quality were purchased and used without further purification, unless stated otherwise. Reactions were monitored by thin-layer chromatography (TLC) carried out on 0.25 mm E. Merck silica gel plates (60FS-254) using UV light to visualize the compounds. Column chromatography was performed using silica gel (60 F254, 70–200 mm) as the stationary phase. All melting points were determined in open capillary tubes on a Stuart Scientific SMP3 melting point apparatus and are uncorrected. IR spectra were obtained on a Perkin-Elmer FTIR spectrum 2000 spectrophotometer. ¹H and ¹³C NMR spectra were recorded with either Varian Mercury VX-300, Varian Unity 300 or 500 MHz spectrometers at room temperature. Chemical shifts are given in ppm (δ) downfield from TMS. Coupling constants (J) are in hertz (Hz) and signals are described as follows: s, singlet; d, doublet; t, triplet; br, broad; m, multiplet; ap, apparent etc. High-resolution analysis (TOF) was performed on an Agilent 6210 time-of-flight LC/MS. 3-Methylimidazo[1,5-*a*]pyridine (**3**)¹⁹ and *O*-mesitylenesulfonylhydroxylamine (MSH)²⁰ were prepared following the procedures described in the literature.

2.1.2. 2-(2-Ethoxy-2-oxoethyl)-3-methylimidazo[1,5-*a*]pyridin-2-ium bromide (**4**)

Ethyl bromoacetate (0.081 mL, 0.75 mmol) was added to a solution of **3** (88.1 mg, 0.67 mmol) in dry acetone (2 mL). The reaction mixture was stirred and heated under reflux for 4 h. The reaction mixture was cooled down to room temperature and the product was filtered off to give

a pale brown solid. This solid was washed several times with acetone and Et₂O to give the desired product in 60% yield (120 mg). M.p: 212–214 °C. IR (KBr) ν cm⁻¹: 3106, 2907, 1737, 1655, 1226, 1026, 748, 439. ¹H NMR (300 MHz, DMSO *d*₆) δ 8.48 (dd, *J* = 7.1, 1.1 Hz, 1H), 8.17 (d, *J* = 0.9 Hz, 1H), 7.86 (dd, *J* = 9.0, 1.1 Hz, 1H), 7.35–7.09 (m, 2H), 5.58 (s, 2H), 4.22 (q, *J* = 7.1 Hz, 2H), 3.32 (s, 3H), 1.25 (t, *J* = 7.1 Hz, 3H). ¹³C NMR (75 MHz, DMSO *d*₆) δ 165.8, 135.3, 127.5, 123.5, 122.5, 117.8, 116.5, 113.3, 61.7, 49.0, 13.4, 8.6. HRMS (ESI-TOF) for C₁₂H₁₅N₂O₂⁺ *m/z* (Calc.): 219.1125, *m/z* (Found): 219.1127.

2.1.3. 2-Amino-3-methylimidazo[1,5-*a*]pyridin-2-ium 2,4,6-trimethylbenzenesulfonate (5)

A solution of MSH (242 mg, 1.12 mmol) in dry CH₂Cl₂ (4 mL) was added dropwise to a solution of **3** (99 mg, 0.74 mmol) in dry CH₂Cl₂ (4 mL). The reaction mixture was stirred at room temperature for 5 h. The solid was filtered off and washed with CH₂Cl₂ and petroleum ether to give compound **5** in 67% yield (172 mg). M.p: 241–244 °C. IR (KBr) ν cm⁻¹: 3254, 3053, 2926, 1646, 1559, 1379, 1081, 860, 679. ¹H NMR (300 MHz, DMSO *d*₆) δ 8.37 (d, *J* = 7.1 Hz, 1H), 8.04 (s, 1H), 7.72 (d, *J* = 9.0 Hz, 1H), 7.30–7.15 (m, 3H), 7.09 (t, *J* = 6.2 Hz, 1H), 6.70 (s, 2H), 2.80 (s, 3H), 2.47 (s, 6H), 2.14 (s, 3H). ¹³C NMR (75 MHz, DMSO *d*₆) δ 142.1, 135.7, 135.3, 132.9, 129.3, 125.9, 123.1, 122.4, 117.2, 115.6, 112.0, 22.2 (2C), 19.8, 7.8. HRMS (ESI-TOF) for C₈H₁₀N₃⁺ *m/z* (Calc.): 148.0857, *m/z* (found): 148.0859.

2.1.4. Dibenzo[*f,h*]pyrido[1',2':3,4]imidazo[1,2-*b*]isoquinolin-16-ium bromide (1)

9,10-Phenanthrenequinone (84 mg, 0.4 mmol) and Et₃N (0.055 mL, 0.4 mmol) were added to a suspension of **4** (120 mg, 0.4 mmol) in EtOH (5 mL). The reaction mixture was stirred and heated under reflux for 24 h. The solvent was removed *in vacuo* to give a residue, which was triturated with Et₂O. The residue was washed with Et₂O and cold acetone. The product was purified by flash column chromatography (98:2 CH₂Cl₂/MeOH) on alumina to give the target compound as a yellow solid in 30% yield (47.5 mg). M.p: 280 °C (decomposition). IR (KBr) ν cm⁻¹: 3397, 3026, 1654, 1534, 1427, 1220, 750, 717. ¹H NMR (500 MHz, DMSO *d*₆) δ 10.51 (s, 1H), 9.92 (s, 1H), 9.48 (d, *J* = 7.0 Hz, 1H), 8.82 (d, *J* = 8.4 Hz, 1H), 8.71–8.48 (m, 4H), 8.01 (d,

$J = 9.3$ Hz, 1H), 7.75–7.51 (m, 5H), 7.25 (t, $J = 6.9$ Hz, 1H). ^{13}C NMR (126 MHz, DMSO d_6) δ 152.2, 146.6, 142.1, 138.8, 135.9, 135.5, 133.9, 133.3, 132.9, 132.1, 131.6, 129.4, 129.2, 128.9, 128.8, 126.5, 126.3, 125.8, 125.1, 124.5, 124.3, 123.9, 123.7, 122.3, 119.7, 22.3 (2C), 19.9. HRMS (ESI-TOF) for $\text{C}_{23}\text{H}_{15}\text{N}_2^+$ m/z (Calc.): 319.1230, m/z (Found): 319.1232.

2.1.5. **Dibenzo[*f,h*]pyrido[1',2':3,4]imidazo[1,2-*b*]cinnolin-10-ium 2,4,6-trimethylbenzenesulfonate (2)**

9,10-Phenanthrenequinone (43.2 mg, 0.21 mmol) and sodium acetate (17 mg, 0.21 mmol) were added to a suspension of **5** (60 mg, 0.17 mmol) in EtOH (4 mL). The reaction mixture was stirred and heated under reflux for 24 h. The reaction mixture was cooled down to room temperature. The solvent was removed *in vacuo* to give a residue, which was triturated with cold water and filtered off. The residue was washed with cold water and EtOAc several times. The resulting solid was dissolved in the minimum amount of MeOH and cold Et₂O was added with cooling (ice bath) until a precipitate had formed. The solid was filtered off to give compound **2** in 50% yield (44.2 mg). M.p: 177–179 °C. IR (KBr) ν cm^{-1} : 3044, 1648, 1602, 1519, 1446, 1318, 1187, 1085, 758, 677. ^1H NMR (500 MHz, DMSO d_6) δ 10.52 (s, 1H), 9.53 (dd, $J = 6.9, 0.7$ Hz, 1H), 9.34 (s, 1H), 8.95 (dd, $J = 8.1, 1.2$ Hz, 1H), 8.81 (d, $J = 8.5$ Hz, 1H), 8.72–8.70 (m, Hz, 2H), 8.19 (d, $J = 9.2$ Hz, 1H), 7.91–7.87 (m, 1H), 7.84–7.77 (m, 4H), 7.58 (t, $J = 6.9$ Hz, 1H), 6.70 (s, 2H), 2.47 (s, 6H), 2.13 (s, 3H). ^{13}C NMR (126 MHz, DMSO d_6) δ 146.3, 142.3, 135.6, 135.3, 131.9, 131.8, 131.7, 130.4, 129.9, 129.2, 129.0, 128.4, 128.3, 127.7, 125.4, 124.9, 124.7, 124.5, 124.3, 123.7, 123.4, 121.5, 117.2, 115.7, 113.8, 108.6, 22.2 (2C), 19.7. HRMS (ESI-TOF) for $\text{C}_{22}\text{H}_{14}\text{N}_3^+$ m/z (Calc.): 320.1182, m/z (Found): 320.1159.

2.2. Ligand-DNA binding

2.2.1. Instrumentation.

Absorption spectra were recorded on a UV-Vis Uvikon 941 (Kontron Instruments) spectrophotometer. Steady-state fluorescence measurements were carried out using a PTI Quanta Master spectrofluorimeter equipped with a Xenon flash lamp as a light source, single concave grating monochromators and Glan-Thompson polarizers in the excitation and

emission paths. Detection was performed with a photomultiplier cooled by a Peltier system. Slit widths were selected at 6 nm for both excitation and emission paths and polarizers were fixed at the ‘magic angle’ condition. Fluorescence decay measurements were performed on a time-correlated single-photon-counting FL900 Edinburgh Instruments Spectrometer. A monochromatic NanoLed (Horiba) emitting at 335 nm was used as the excitation source. Double concave grating monochromators were employed at both excitation and emission paths. Photons were detected by a red-sensitive cooled photomultiplier (by a Peltier system). The data acquisition was carried out by using 1024 channels of a multichannel analyzer with a time window width of 200 ns. A total of 10,000 counts in the maximum peak channel were taken for each measurement. The instrumental response function was regularly achieved by measuring the scattering of a Ludox solution. Intensity fluorescence profiles were fitted to multi-exponential decay functions by using the iterative deconvolution method.²¹ Right angle geometry and rectangular 10 mm path cells were used for all the absorption and fluorescence measurements.

Circular dichroism spectra at 25 °C were obtained on a JASCO-715 spectropolarimeter. Recorded spectra were the average of 3 scans taken at a speed of 50 nm·min⁻¹ with a 0.125 s time response. The sensitivity and resolution were fixed at 20 mdeg and 0.5 nm, respectively. Measurements were performed on samples in a 0.1 cm (1 cm) path quartz cell while monitoring the CD (ICD) spectra in the region where DNA (ligand) mainly absorbs.

2.2.2. Thermodynamics. The association constant K of a fluorescent ligand (L) to n effective binding sites of large molecule (M) under the assumption that these n binding sites of M per ligand (L) are independent and equivalent and can be related to the fluorescence intensity (I) by the following equation:

$$I = I_0 + (I_\infty - I_0) \times \frac{(1 + nK[L]_0 + K[M]_0) - \sqrt{(1 + nK[L]_0 + K[M]_0)^2 - 4nK^2[L]_0[M]_0}}{2Kn[L]_0} \quad (1)$$

where $[M]_0$ and $[L]_0$ are the initial concentrations of M and L .

The normalized difference between the fluorescence intensity (I) for L in the presence of M and in its absence (I_0), can be written as:

$$\frac{\Delta I}{I_0} = \left(\frac{I_\infty - I_0}{I_0} \right) \times \frac{(1/[L]_0 + nK + KR) - \sqrt{(1/[L]_0 + nK + KR)^2 - 4nK^2R}}{2Kn} \quad (2)$$

where R is the $[M]_0/[L]_0$ molar ratio. As M corresponds to DNA, $[M]_0$ is the DNA concentration per mol of base pairs and n is the number of base pairs per bound ligand molecule. Equations are derived in the ESI.

2.2.3. Modeling. The minimum binding energy (MBE) structure for the L/DNA complex was obtained by sequentially approaching each ligand (depicted in **Figure 1**) to a DNA fragment containing twelve CGCGAATTCGCG sequence nucleotides (percent of the ctDNA bases) by the major groove, with their center of mass on the y axis in a coordinate system as depicted in Figure 2. The possibility of binding to grooves was not considered as a result of the ICD spectra intensity and sign obtained. Optimized MBE structures for the **1/** and **2/DNA** complexes were used as starting conformations for Molecular Dynamics (MD) simulations. Histories of several parameters related to the structure of the complexes were obtained from the analysis of MD trajectories. Calculations were performed with Sybyl X-2.0²² and the Tripos Force Field.²³ Further details and protocols for these calculations are described in the supporting information and elsewhere.^{13c,16,24}

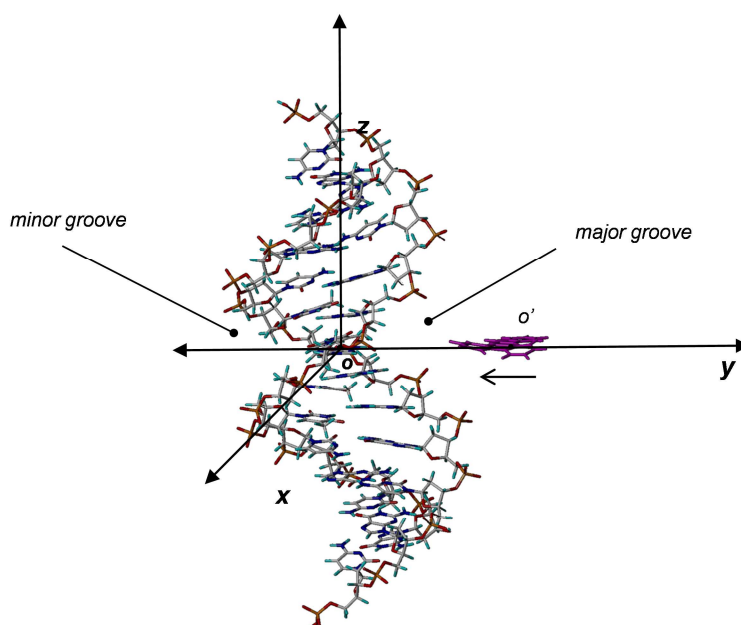


Figure 2. Cartesian system used to define the L-to-DNA approach. The pair of central AT and TA bases were almost parallel to the xy ligand plane. The most favorable L orientation is depicted.

2.2.4. Materials for titrations. Stock concentrated solutions of ligands **1** and **2** were dissolved in DMSO (Aldrich, HPLC grade) and diluted with a phosphate-buffered saline solution (PBS) at pH = 7.4 to reach concentrations in the 10^{-5} molar concentration range. The final solutions contained 5% DMSO. A 2 mg/mL calf thymus DNA (ctDNA, high molecular weight sodium salt, Aldrich) solution was prepared in Milli-Q water. For titration purposes a ctDNA of 2.36×10^{-3} mol/per base pair stock solution was prepared in the buffer from the previous solution. This concentration (per pair of bases) was determined by UV-Vis ($\epsilon_{260\text{nm}} = 13,200 \text{ M}^{-1}\text{cm}^{-1}$).²⁵ For titrations, aliquots of this stock DNA solution were added to a 10 mm quartz cuvette containing 2.5 mL of the above ligand solution. After each addition the content was stirred for approximately 10 minutes. The titration reached **1**/ and **2**/DNA base pair molar ratios of approximately 1:7 and 1:3, respectively. The effect of the ligand dilution never represented more than 5% error on the ligand concentration.

2.3. Thermal denaturation experiments

Melting curve studies were carried out following previously described procedures.^{13c,16, 26} Synthetic oligodeoxynucleotides with one strand 5'-end labeled with the fluorophore 6-carboxyfluorescein (6-FAM, F) and the complementary strand 3'-end labeled with the fluorescence quencher tetramethylrhodamine (TAMRA, Q) were synthesized by Bonsai Technologies Group S.A. (Avda. Valdelaparra 27, 28108 Alcobendas, Madrid, Spain) on either the 0.2 or 1 μmol scale and were purified by high-performance liquid chromatography to give a single peak. Annealing of each F oligonucleotide with its complementary Q oligonucleotide at a final duplex concentration of 0.1 μM in TAE buffer (0.08 M Tris-acetate, 2 mM EDTA, pH 7.5) was accomplished in a PTC-100 thermocycler (MJ Research, Inc. Waltham, MA) by first heating to 95 °C for 5 minutes and then gradually cooling to 20 °C at a rate of 1 °C min^{-1} . Correct annealing was confirmed because when the oligonucleotides form a double-stranded structure, F and Q are placed in proximity so that the fluorescence of F is quenched. The melting reactions were carried out in 96-well plates loaded with the double-stranded

preannealed oligonucleotides in a total volume of 20 μL of TAE buffer at a final concentration of 0.1 μM either in the absence or in the presence of the compound under study. The compounds were dissolved in dimethyl sulfoxide and serially diluted in the same solvent to yield final concentrations in the range from 10^{-5} to 10^{-8} M. The mixtures were incubated in all cases for 60 minutes at 37 $^{\circ}\text{C}$ before the melting assay was started in a 7500 Fast Real-Time PCR System (ABI Prism, Applied Biosystems) by increasing the temperature in small steps of 1 $^{\circ}\text{C min}^{-1}$ up to 95 $^{\circ}\text{C}$. Upon heating, a temperature is reached at which the double strand melts so that groups F and Q are separated and the fluorescence increases. By recording the changes in fluorescence at 517 nm in the FAM channel obtained as a function of temperature and calculating the midpoint of the transition (T_m), we were able to estimate the increases in melting temperatures (ΔT_m) brought about by ligand binding at increasing ligand concentrations. The following oligonucleotides were used: 5'-F-d(CAATTAAATATAAC) and 5'-F-d(GCGCGGCGTCCGGGCC), together with their respective 3'-Q-labeled complementary strands. These sequences were designed to provide nearly all of the possible subsequences of four bases formed by A and T or G and C, respectively, that could be recognized by the compound while at the same time minimizing the possibility of incorrect annealing. The raw data recovered from the instrument for each plate consisted of an array of FAM fluorescence values for each of the 96 wells at each temperature.

2.4. Live-cell studies

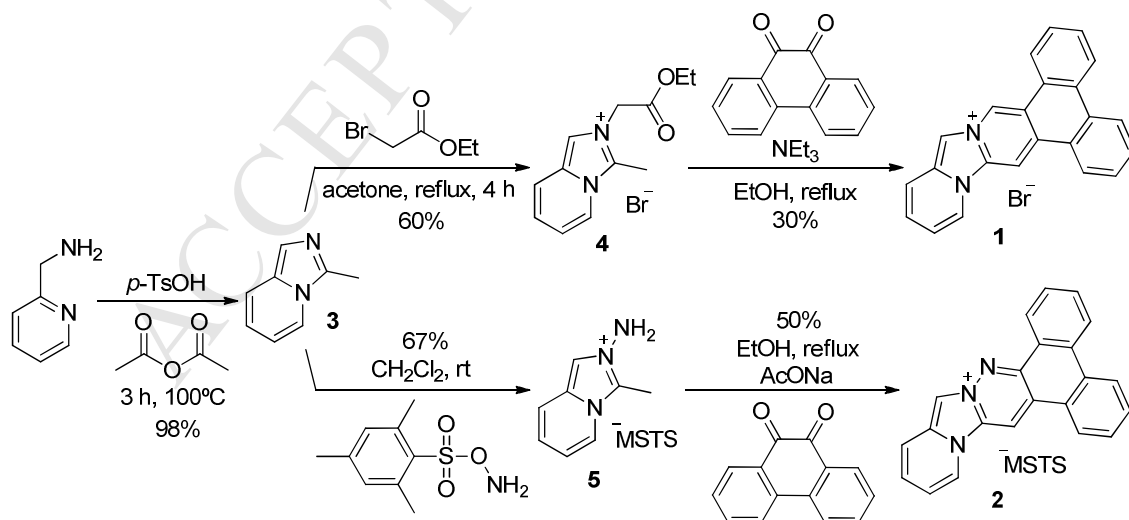
HeLa cells were maintained at 37 $^{\circ}\text{C}$ and 5% CO_2 in Dulbecco's modified Eagle's medium (DMEM) supplemented with 10% fetal calf serum and 100 units/mL penicillin and streptomycin. For live-cell staining, cells were grown on coverslips and stained by addition of the compound under the conditions indicated in each case. Static images and time-lapse video recordings were obtained using a BioRad confocal microscope. Cytotoxicity experiments were carried out using the standard 3-(4,5-dimethylthiazol-2-yl)-2,5-diphenyltetrazolium bromide (MTT) assay.²⁷ The cells were seeded into a 24-well plate at a density of 1.5×10^4 cells per well and incubated in medium containing the compound under study at different concentrations for

24 or 48 hours. To each well, 100 μL of MTT was added and the plates were incubated at 37 $^{\circ}\text{C}$ for 4 hours to allow MTT to form formazan crystals on reacting with metabolically active cells. The medium with MTT was removed from the wells. Intracellular formazan crystals were dissolved by adding 100 μL of DMSO to each well and the plates were shaken for 10 minutes. The absorbance was recorded using a multiwell plate reader.

3. Results and discussion

3.1. Synthesis of cations **1** and **2**

Compounds **1** and **2** were readily obtained in three steps from commercially available 2-aminomethylpyridine. In this way, this starting material was treated with acetic anhydride and *p*-toluenesulfonic acid to give the methylimidazopyridine **3**,¹⁹ which was aminated using *O*-(mesitylsulfonyl)hydroxylamine (MSH)²⁰ to give derivative **4** or alkylated using ethyl bromoacetate to give derivative **5**. Finally, **4** and **5** were reacted with 9,10-phenanthrenequinone and base in a Westphal condensation to give the desired chromophores **1** and **2**. It is worth noting that the Westphal reaction of **4** produced product **1** with loss of the ester group as a result of *in situ* hydrolysis and decarboxylation.^{18a}



Scheme 1. Synthesis of cations **1** and **2**

3.2. Ligand-DNA binding

3.2.1 Absorption and emission spectra. The values for the absorption maxima and molar absorptivities at the excitation wavelength (λ_{ex}) used for monitoring the emission spectra of **1** and **2** in a 5% DMSO/water mixture and in methanol are provided in **Table 1**. The absorption spectra for dilute solutions of ligands **1** and **2** in a 5% DMSO/water mixture at 25 °C are shown in **Figure 1S** (ESI). The spectra in **Figure 3** represented by dashed lines (also in Figure 2S of ESI) correspond to ligands **1** and **2** in very dilute (3.0×10^{-5} and 2.31×10^{-5} mol/L concentrations, respectively) buffer (5% DMSO) solutions with λ_{ex} of 440 and 470 nm, respectively. The spectrum of **1** contains a band at ~515 nm and this is accompanied by a shoulder at 488 nm. In the case of **2**, however, a single band centered at ~538 nm can be observed. The fluorescence quantum yields are summarized in Table 1 and these were obtained using a Rhodamine 101 (inner salt, Sigma-Aldrich, for fluorescence) solution in ethanol as standard for both compounds in 5% DMSO/water and methanol at 25 °C.²⁸

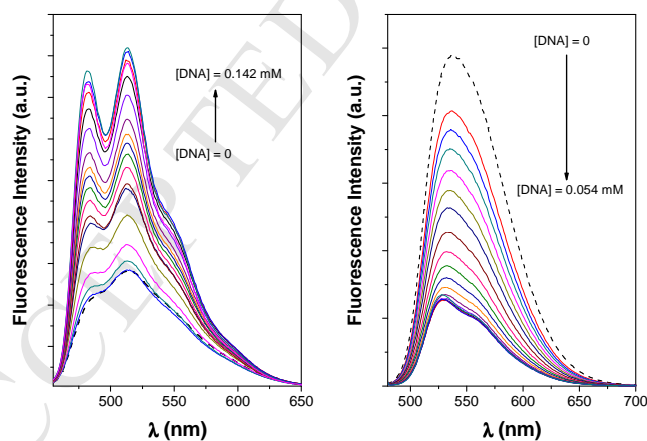


Figure 3. Emission spectra at 25 °C for ligands **1** (left) and **2** (right) in buffer solutions ($[L] = 3.0$ and 2.31×10^{-5} mol/L, respectively) and upon the addition of aliquots of DNA.

Hardly any shift of the emission maxima was observed upon DNA addition during the titration experiments for any of the ligands. However, as shown in **Figure 3**, significant changes in the fluorescence intensity were observed. A fluorescence enhancement was observed during the

titration of **1** whereas intensity quenching was observed for **2**. Furthermore, the spectrum of **1** exhibited a new band at ~ 482 nm, the intensity of which increased upon addition of DNA. A small shoulder was also evident at ~ 560 nm, but this also appeared in the spectrum of **2**. Excitation spectra (**Figure 3S**, ESI) recorded at the maximum emission intensities for **1** and **2** exhibited features similar to those in the corresponding absorption spectra; an increase and a decrease in the intensity of the spectra were observed upon DNA addition for **1** and **2**, respectively.

The observations outlined above indicate a binding interaction for both ligands with DNA. The normalized variation of the fluorescence intensity of **1** and **2**, as $(I - I_0)/I_0$ (I is the integral of the emission band and the subscript zero signifies in the absence of DNA), versus DNA/L molar ratios is depicted in **Figure 4**. Similar representations obtained from the intensities measured at the maximum of the low energy bands from the excitation spectra of **1** (440 nm) and **2** (460 nm) are depicted in the supporting information (Figure 3S). **Figure 4S** in the supporting information also shows the variation of the fluorescence anisotropy r (eq 10S, ESI), monitored at the emission maximum upon excitation at the same wavelength where the emission spectra were collected, versus molar ratios at 25 °C.

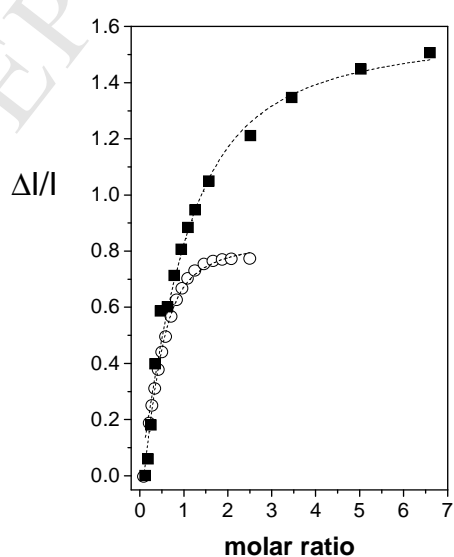
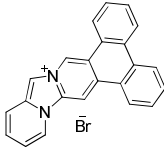


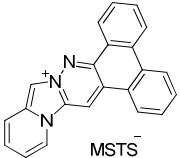
Figure 4. Normalized variation of the fluorescence intensity for ligands **1** (■) and **2** (○) in 5% DMSO and 95% buffer solutions ($[1] = 3.0 \times 10^{-5}$ and $[2] = 2.31 \times 10^{-5}$ mol/L) at 25 °C versus DNA/ligand molar ratios (R) during titrations.

The r values for solutions of **1** and **2** at 25 °C in the absence of DNA denote different orientations of the absorption and emission transition moments, molecule sizes and/or rotational diffusion in a low viscosity aqueous solvent at 25 °C. The r values for **1** and **2** increased significantly with [DNA], which is a typical trend for the formation of **1**:DNA and **2**:DNA complexes whose rotational relaxation times are larger when compared to those of the free ligands **1** and **2**.²⁹

The curves depicted in **Figure 4** for titrations of **1** and **2** are the result of the fitting of the experimental data to equation 2. This provides a value for the binding constant of ca. $(6.7 \pm 3.6) \times 10^4 \text{ M}^{-1}$ for **1**. This value is of the same order of magnitude as those for some other derivatives of quinolizinium DNA intercalators previously reported by us and others.^{7,16} The average number of nucleic base pairs per bound ligand was 0.9 ± 0.4 . However, compound **2** exhibited an association constant of $(4.5 \pm 1.1) \times 10^5 \text{ M}^{-1}$, which is one order of magnitude larger, and a surprising n value of 0.6 ± 0.1 , which denotes strong DNA-**2** interactions. The curves shown in **Figure 3S** in the supporting information were obtained from excitation spectra and these reproduce the adjustment to equation 2 by using K and n values previously obtained from analysis of the emission spectra.

Table 1. Selected photophysical data in 5% DMSO/water and in methanol (parentheses) at 25 °C. Fluorescence quantum yields (ϕ_f) were obtained by using Rhodamine 101 in ethanol as a standard.²⁸

Code	Structure	Absorption spectra (peaks and shoulders), λ_{ex}	ϵ ($\text{M}^{-1}\text{cm}^{-1}$) in 5% DMSO/water at λ_{ex} (in methanol at 458 nm)	ϕ_f at λ_{ex}	$\lambda_{\text{em, max}}$ (nm)
1		244(p),280(p), 299(s),340(s), 365(p),385(p), 416(s), 440(p),463(s)	2580 (3,440)	0.17 (0.16)	528

2	 MSTs ⁻	246(p),279(s), 314(p),340(s), 358(s),441(s), 470(p) ,485(s) 470	8940 (5,570)	0.32 (0.46)	536
---	--	--	--------------	-------------	-----

Fluorescence intensity decay profiles for ligands **1** and **2** were fitted to double exponential functions with lifetime components of 6.9 ns (9.4 ns) and 17.1 ns (26.1 ns) for ligand **1** (**2**) and a weighted average lifetime ($\langle\tau\rangle$) of 8.9 ns (10.0 ns) (see ESI for $\langle\tau\rangle$ definition).³⁰ The presence of DNA makes the profiles more complex (the sum of three exponential decays). In addition, a decrease in $\langle\tau\rangle$ with the DNA/L molar ratios was observed for both complexes, as shown by the data in **Table 2**. This decrease is more significant for ligand **2**.

Table 2. Lifetime for the ligands in 5% DMSO and 95% buffer solutions in the absence and in the presence of DNA at different DNA/ligand molar ratios at 25 °C. A NanoLed emitting at 335 nm was used as the excitation source.

DNA/L ratios	$\langle\tau\rangle$, ns	DNA/L ratios	$\langle\tau\rangle$, ns
L = 1		L = 2	
0	8.9	0	10.0
0.4	7.9	0.5	8.4
0.8	7.6	1.0	8.3
1.2	7.4	1.5	7.5
1.6	7.4	2.5	5.5
2.4	7.4	4.0	5.8
3.1	7.3		

3.2.2 Circular dichroism measurements. The circular dichroism (CD) spectrum in the region of the DNA absorption provides information about alterations in its secondary structure upon L to DNA interaction.³¹ As can be seen in **Figure 5**, ctDNA shows the typical B-form CD spectrum with positive and negative Cotton effects centered at ~278 and ~245 nm. Bands are attributed to base stacking and right-handed polynucleotide helicity, respectively. Changes in both bands are

usually sensitive to the mode of interaction with small molecules.³² Some authors state that while groove binding and the electrostatic interaction of small molecules with DNA show little or no perturbations in both bands, intercalation due to strong base stacking interactions and stable DNA conformations usually enhances their intensities. Some other authors, however, assert that intercalated complexes that disrupt interactions between bases should cause a decrease in the observed band intensities.³³ As depicted in **Figure 5**, the intensities of both bands decrease upon increasing the concentration of **1**. Compound **2**, however, exhibits a decrease in the intensity of the band located at 245 nm and an increase in the band at 278 nm.

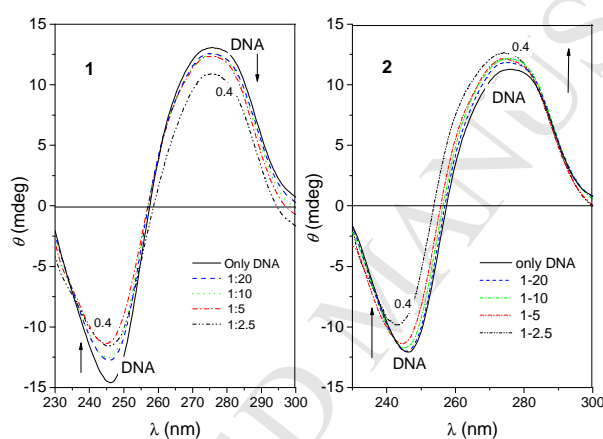


Figure 5. CD spectra (ellipticity, θ) in the region of DNA absorption at 25 °C for ligands **1** (left) and **2** (right) in 5% DMSO and 95% buffer solutions in the presence of DNA ($[DNA] = 7.20 \times 10^{-4} M$ and $6.70 \times 10^{-4} M$, respectively) at several ligand/DNA molar ratios.

However, as ligands **1** and **2** both also absorb in this region, an ICD signal from the DNA/L complex would also appear in this zone. This is undoubtedly observed in the CD spectra for ligand/DNA solutions at very low DNA concentrations (**Figure 5S of ESI**). As a consequence, we believe that the CD spectra in this region consist of the overlapping of both CD and ICD spectra from DNA and L complexed, respectively, which casts doubt on previous conclusions reported by other authors.^{32,33} The observation of an ICD spectrum at $\lambda \geq 300$ nm, i.e., in the region where **1** and **2** predominantly absorb and DNA does not, is a consequence of ligand complexation with DNA. The magnitude and sign of the ICD spectrum depends on the orientation of the transition moment inside the intercalation site and on the lateral displacements of the intercalator relative to

the helix axis. An intercalator exhibits a weak negative ICD when the transition moment for the corresponding absorption band is oriented along the long axis of the binding DNA pocket (parallel to the bisector of the base pairs or perpendicular to the pseudo-dyad axis). However, a positive strong ICD is expected when the transition moment is perpendicular to the long axis of the binding pocket. The ICD signal for a groove-bound ligand is positive and one or two orders of magnitude larger than for an intercalated ligand.^{7,31a,34}

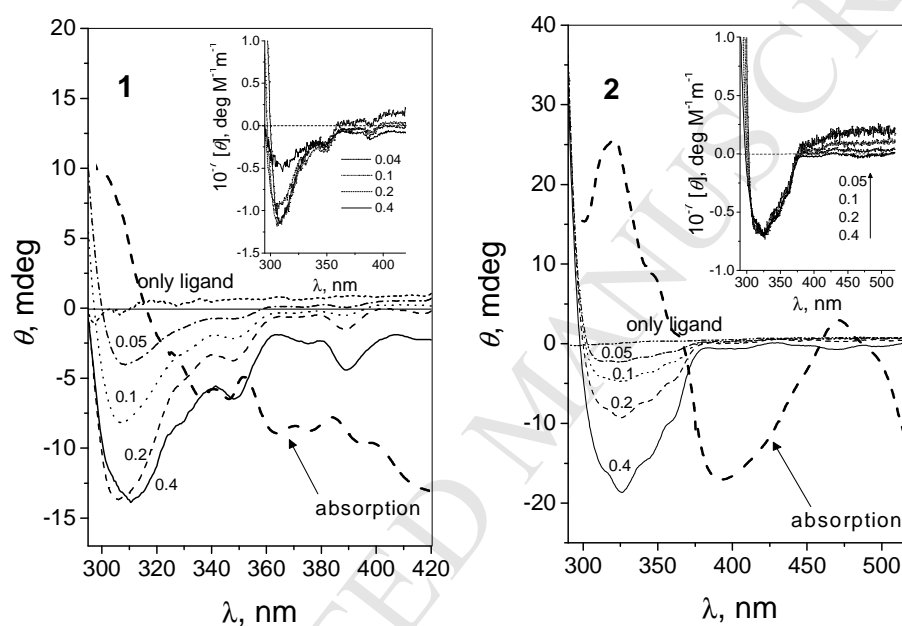


Figure 6. Ellipticity θ for ligands **1** and **2** in 5% DMSO and 95% buffer solutions in the presence of DNA ($[DNA] = 7.20 \times 10^{-4}$ M and 6.70×10^{-4} M, respectively) at several ligand/DNA molar ratios at 25 °C. The CD spectra, represented as molar ellipticity, are superimposed. Also superimposed are the absorption spectra for ligands **1** and **2** (---, black).

The ICD spectra for isolated **1** and **2** in solution and in the presence of DNA at different L:DNA molar ratios, at constant $[DNA]$, are shown in **Figure 6**. No signals were observed for isolated **1** and **2**. However, CD spectra for **1**/DNA or **2**/DNA solutions at any of the ratios used exhibit Cotton effects, albeit with relatively low intensity, with the intensities depending on the ligand concentration. The spectra for **1**/DNA and **2**/DNA solutions at any of the ratios are also consistent with the absence of exciton coupling, which excludes a ligand aggregation during association to DNA.^{7,34} Molar ellipticity $[\theta]$ allows visualization of the ICD spectra in two different regions and

these correspond to distinguishable bands that appear in the absorption spectra. For ligand **1**, one of these bands, which is negative, extends below ~ 350 nm; the other one, which is almost zero, covers wavelengths greater than ~ 350 nm. However, this wavelength limit between the two bands occurs at around 380 nm for **2**. The ICD spectrum for the high energy band of **2** is also negative, whereas the signal for the low energy bands is slightly positive. Assuming that the transition moments of the bands that appear at lower wavelengths are almost perpendicular to the long ligand axis, the negative sign of the ICD bands reveals an intercalation of ligands **1** and **2** with their short-molecular axis preferentially parallel to the DNA binding pocket.^{7,31a,34a} However, the virtual absence or slight positive sign of the ICD signal for the low energy band (attributed to interaction with the ligand transition moment oriented nearly along the long ligand axis) must agree with a transition moment oriented at nearly 45° (or slightly $<45^\circ$) to the base pair binding pocket. The absence of large positive θ values also excludes the presence of groove binding ligand/DNA interactions.

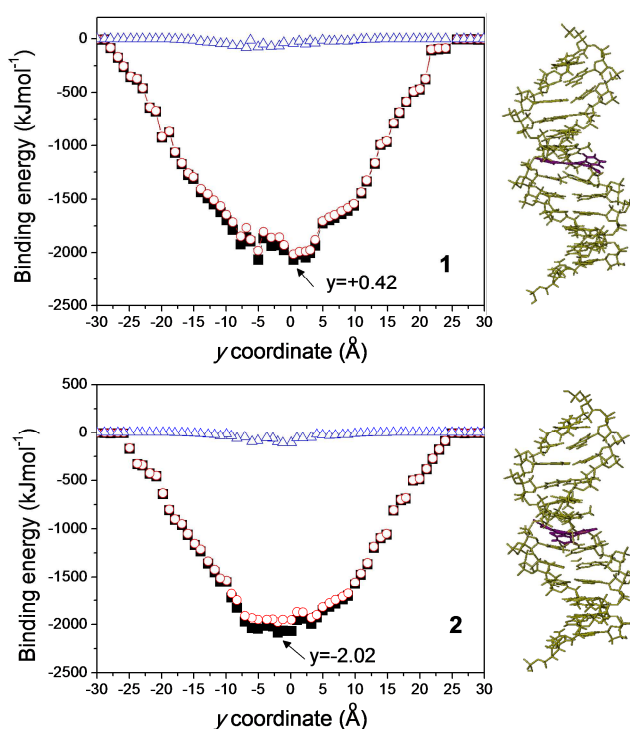


Figure 7. Total binding energies (□) and van der Waals (△) and electrostatic (○) contributions as a function of the oo' distance measured along the y coordinate for ligands **1** and **2** approaching DNA as intercalators. The MBE structures for **1** and **2** are represented and, once minimized again, these were used as starting conformations for the MD simulations.

3.2.3 Molecular mechanics and molecular dynamics. The total energy binding energy is depicted in **Figure 7** along with the van der Waals and electrostatic contributions for **1** and **2**, with the most favorable orientation intercalating the DNA by the major groove parallel to the plane bases as a function of the oo' distance along the y coordinate. Intercalation takes place with no significant potential barriers. It can be seen from **Figure 7** that electrostatic interactions are mostly responsible for the stabilization. Minima binding energy (MBE) structures for **1**/DNA and **2**/DNA complexes obtained by MM calculations are also depicted. Compound **1** intercalates in such a manner that its main axis is oriented around 45° to the TA and AT central basis binding pocket and is slightly outside the major groove face. However, the main long axis of **2** is almost parallel to the bases pocket axis and slightly outside the minor groove face.

Analysis of the 1.0 ns MD trajectories at 300 K on the water-solvated MBE optimized structures depicted in **Figure 7** showed that ligand-DNA interactions are favorable for both intercalations throughout the whole trajectory (**Figure 6S, ESI**). As with MM, the most important contributions to stabilization are electrostatic. The van der Waals contribution represents barely 10% of the total binding energy.

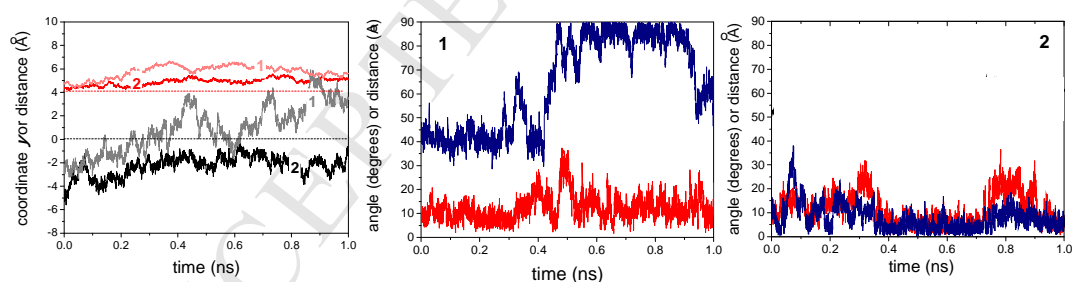


Figure 8. (Left panel) Histories for the y coordinate (bottom lines) for the center of **1** (black) and **2** (gray) ligands (o') and the end-to-end DNA helix distance per nucleotide unit (upper red lines) for **1**/DNA (red) and **2**/DNA (light red) complexes obtained from the analysis of the 1 ns MD trajectory at 300 K starting from the minimized MBE structures. Dashed lines are the values for the initial structures. (Middle and right panels) Histories for the averaged angles between the plane of both AT and TA pairs of bases and the plane of the **1** (middle) or **2** (right) ligand rings (red) and the angle between the bisector of pocket bases and the long ligand axis (blue) from the analysis of the MD trajectories.

The histories for the y coordinates of the center of ligands are depicted in the left-hand panel of **Figure 8**. The MBE structure at time zero and at the end of the trajectory for the **1**/DNA complex is represented in **Figure 9**. The **1** (**2**) intercalator tends to move early inside the base pair pocket close

to the y coordinate zero and is slightly outside the major (minor) groove side. The averages of the y coordinate throughout the MD trajectories were 0.9 ± 2.0 and -2.3 ± 0.9 Å, respectively. This movement also involved some rotation in the case of **1** and a subsequent increase in the angle between the binding pocket axis and the long axis of **1**. In fact, after ~ 0.45 ns **1** was oriented almost perpendicular to the pocket with the phenanthrene group lying slightly outside the pocket by the major groove face (see **Figure 9**) to decrease the angle slightly at the end of the trajectory. The average of the binding pocket axis and the long axis angle throughout the trajectory was $64\pm 20^\circ$, which is reasonably consistent with the weak negative high energy band whose transition moment was assumed to be nearly perpendicular to the long axis of **1**. The average of the angle between the binding bases pocket and the long axis of the ligand **2**, however, was $8\pm 5^\circ$, which means that it does not reproduce the signs and intensity of the bands monitored in the ICD spectrum for **2**/DNA solutions.

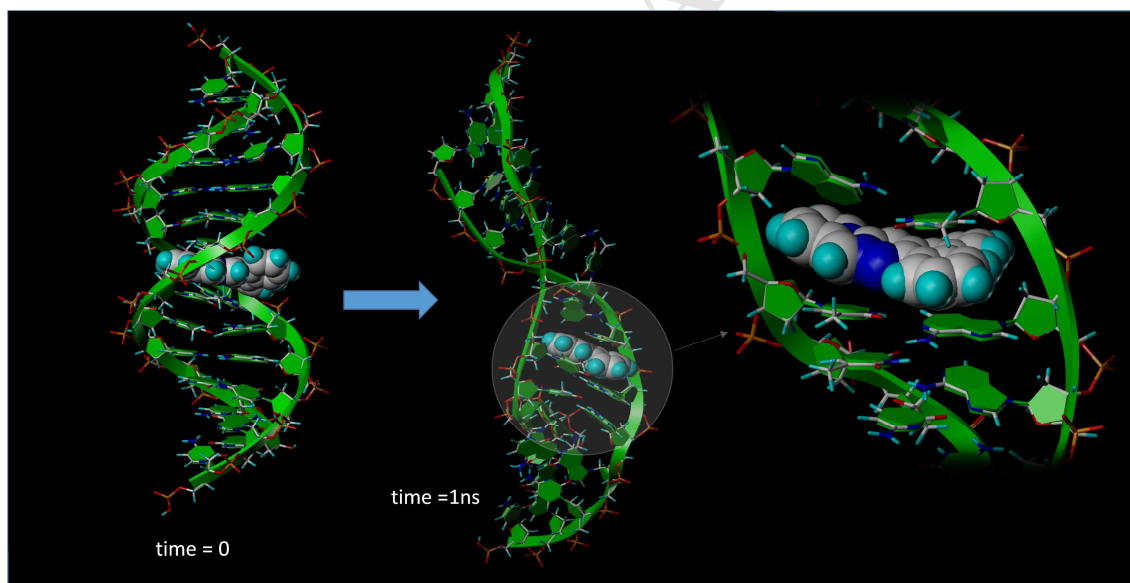


Figure 9. Snapshots of the 1 ns MD trajectory at 300 K showing the location of ligand **1** at time = 0 ns and at 1 ns from the beginning of the trajectory. Detail of the location of ligand **1** at the end of the 1 ns trajectory (right).

In addition, the angles between the AT and TA base pair planes and the plane of both ligands **1** and **2** were close to zero (averages of $12\pm 6^\circ$ and $11\pm 7^\circ$, respectively) – as one would expect for ligands

that intercalate. Another characteristic upon intercalation is the distortion of the DNA double helix and a slight unwinding and lengthening of the DNA chains. In fact, from the initial DNA fragment, whose end-to-end DNA distance per nucleotide unit was 4.1 Å, the intercalation led to an increase in this value to 5.8 ± 0.5 Å and 4.9 ± 0.3 Å for **1**/DNA and **2**/DNA complexes, respectively. The latter values correspond to the averages over the entire trajectory.

A longer trajectory of up to 3 ns complex was performed for **2**/DNA. The analysis showed how the average of the angle between the binding bases pocket and the long axis of **2** increase with time (**Figure 7S**, ESI). Indeed, after ~ 2 ns of the trajectory ligand **2** rotated slightly in such a manner that the angle between the long axis and the binding pocket increased and even reached values of $\sim 70^\circ$. The average of this angle during the last nanosecond of the trajectory was $40 \pm 9.0^\circ$. The structures for the **2**/DNA complex at the end of the 3 ns trajectory are shown in **Figure 8S** of the ESI.

3.3. Thermal denaturation experiments

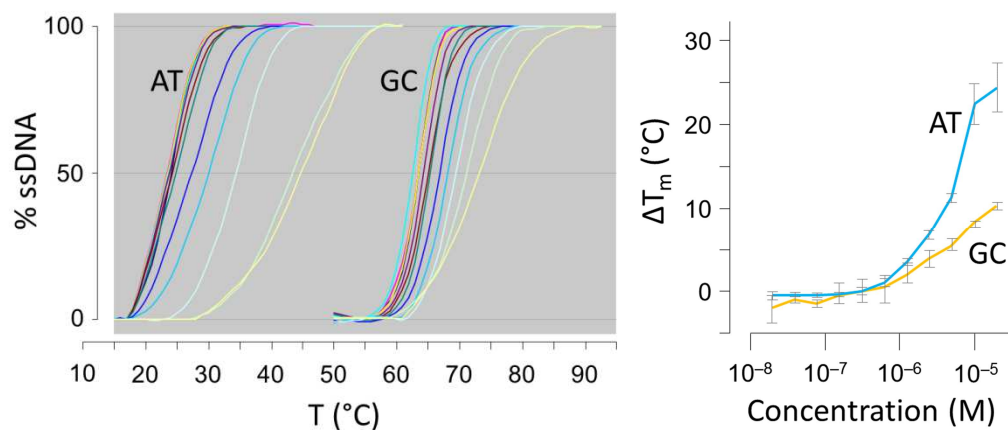


Figure 10. Melting curves (left panel) and plot of the experimental ΔT_m versus ligand concentration on a logarithmic scale (right panel) obtained for reaction mixtures of compound **2** and double-stranded DNA oligonucleotides of different base compositions and sequences. Oligonucleotide AT (blue line).- 5'-CAATTAAATATAAC-3' and its complementary. Oligonucleotide GC (orange line).- 5'-GCGCGCGTCCGGGCC-3' and its complementary. Each data point is the average of two separate experiments. Ligand concentrations (M): 1.95×10^{-8} , 3.91×10^{-8} , 7.81×10^{-8} , 1.56×10^{-7} , 3.13×10^{-7} , 6.25×10^{-7} , 1.25×10^{-6} , 2.5×10^{-6} , 5.0×10^{-6} , 1.0×10^{-5} and 2.0×10^{-5} .

DNA binding studies on compound **2** were carried out by FRET-based thermal denaturation experiments using custom synthetic oligonucleotides with defined AT- or GC-rich sequences (**Figure 10**). The duplex containing the GC-rich sequence (GC) produced a simple monophasic profile with a melting temperature (T_m) of 62 °C, which changed slightly and gradually upon addition of increasing concentrations of **2**. In fact, at a ligand concentration of 20 μ M, the ΔT_m reached a maximum of ~ 10 °C. In contrast, the T_m of the AT-rich oligo, AT, rapidly increased upon addition of **2** and the melting curve was shifted by almost 24 °C at the same concentration of 20 μ M (**Figure 10**). This difference suggests a preference of **2** for DNA sequences that are rich in AT base-pairs.

3.4. Live-cell studies

The toxicity of compounds **1** and **2** on living cells in culture was determined by the standard MTT assay using the HeLa cell line after 24 and 48 hours of exposure. The apparent lethal dose 50% (LD_{50}) is close to 1.0×10^{-5} in all cases (see ESI).

The capacity of compounds **1** and **2** for live-cell staining, uptake and intracellular distribution was studied by confocal microscopy imaging and time-lapse video recording, using HeLa cells grown on coverslips in Dulbecco's Modified Eagle's Medium supplemented with 10% fetal bovine serum (DMEM, 10% FBS). The analysis showed the remarkable capacity of both compounds for uptake and accumulation by living cells. Cells treated with compound **1** showed a disruption of internal structures and a fluorescent staining compatible with apoptotic fragmentation of the nucleus (**Figure 11**, upper panels). On the other hand, compound **2** showed a clear staining pattern of interphase nuclei and metaphase chromosomes (**Figure 11**, lower panels).

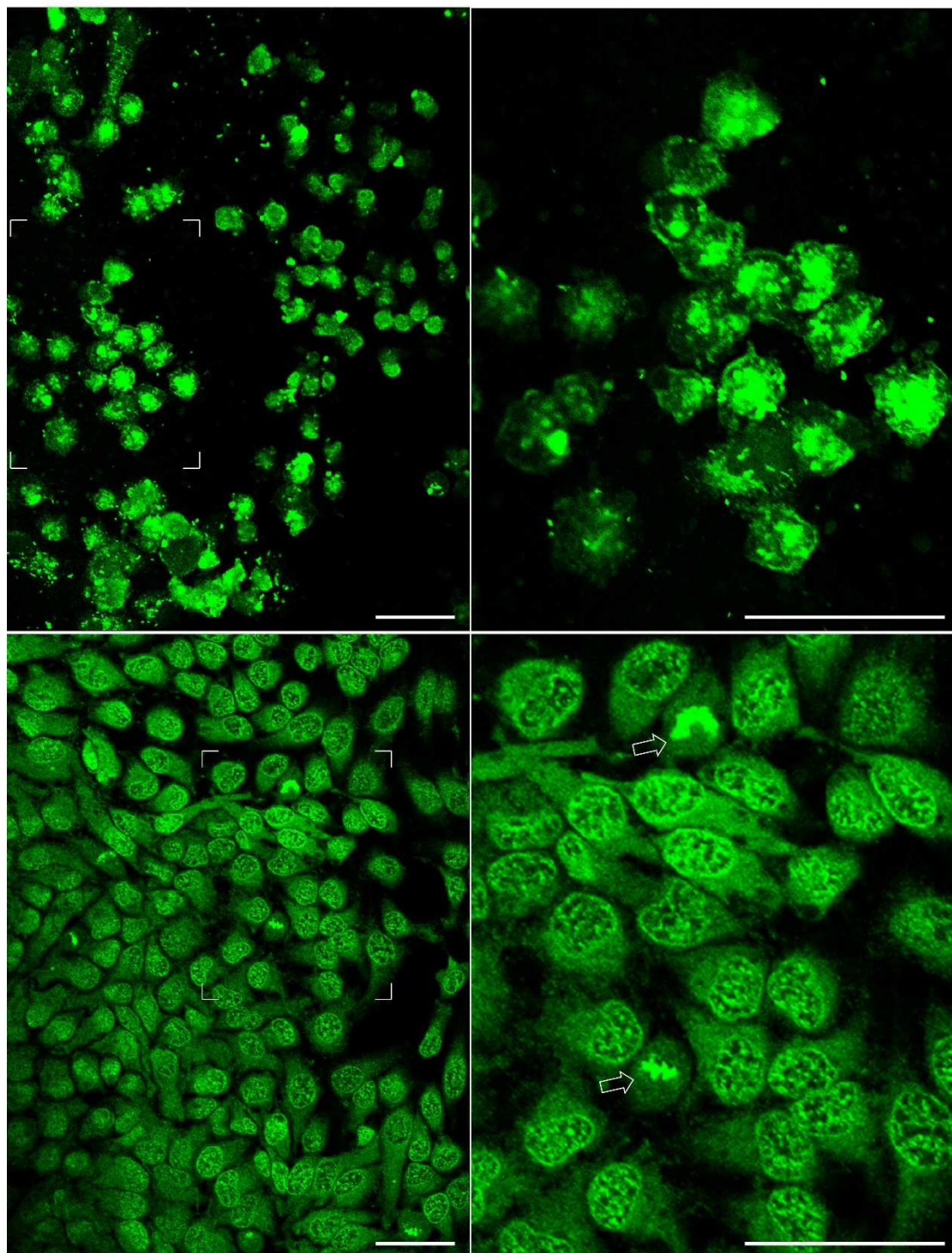


Figure 11. Living HeLa cells in culture after 1 hour of exposure to compounds **1** and **2**. Upper panels: compound **1**, 12.80 mM in DMSO, diluted 1:400 in culture medium (32 μ M final). Lower panels: compound **2**, 56.70 mM in DMSO, diluted 1:400 in culture medium (142 μ M final). Confocal microscopy images (excitation argon laser 488 nm, emission filter 500–575 nm). Left panels: wide field with corner marks indicating the area magnified on the right. Lower right panel: detail of a region with two cells in mitosis (arrows) showing bright fluorescent chromosomes in metaphase plates stained with compound **2**. The scale bar represents 50 μ m in all panels.

The uptake and intracellular distribution of compound **2** appears to be a complex process and is apparently due to active biological accumulation rather than passive diffusion and binding. The final staining is strongly concentrated inside the nuclei. Mitotic metaphase chromosomes are also brightly stained (**Figure 11**, lower panel).

The intracellular and nuclear staining patterns were complex and clearly change at different incubation times. After experiments at fixed incubation times, it was decided to investigate the complete dynamic process by time-lapse video recording using a confocal microscope equipped with a thermostatic chamber. A composition made with selected frames in order to follow the changes in a set of cells is shown in **Figure 12**.

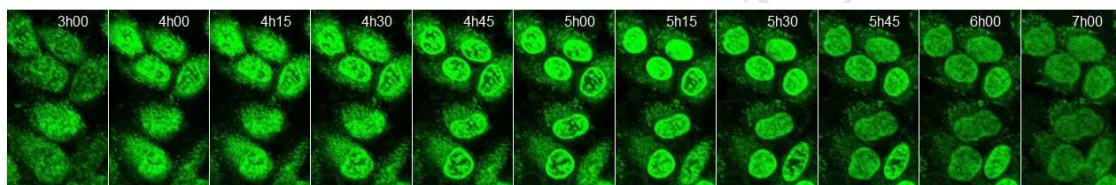


Figure 12. Frames selected from a time-lapse, confocal video microscopy recording of living HeLa cells in culture exposed to compound **2**, 56.70 mM in DMSO, diluted 1:1000 in culture medium (56.7 μ M final). The complete sequence was recorded at 2 frames per minute. Excitation argon laser 488 nm, emission filter 500–575 nm, gain settings were kept constant during the recording.

In the initial steps, the fluorescence is accumulated in disperse, vesicle-like cytoplasmic structures, which is compatible with an active endocytic mechanism rather than passive diffusion of the compound through the plasma membrane. A progressive increase is clearly visible in the time-lapse video recording. The nucleus is initially not differentiated but the fluorescence subsequently begins to increase inside. The nuclei become very brightly stained, with a reproducible pattern of fluorescence accumulation in the periphery and defined internal areas, apparently concentrating most of the compound within the cell. The stained nuclei undergo dramatic structural changes. Initially they appear to collapse and acquire a round shape, with an apparent reduction in diameter following a progressively homogeneous, compact and bright staining. After a short time the diameter of the nuclei begins to increase and the internal

fluorescence gradually fades away. At this stage the content of the nuclei appears homogeneous, with an apparent loss of all internal structures but without signs of apoptotic fragmentation.

The same process occurs in all of the cells and follows the same sequence and timing, but it is not synchronous in different cells. A clear example can be seen in the two cells near to the lower edge of the frames in **Figure 12**. This feature indicates the participation of some active cellular process in the uptake and accumulation rather than a simple diffusion and binding of the compound.

Once the compound enters the nucleus, very likely through the nuclear pores, the fluorescence pattern suggests strong binding to DNA and a progressive accumulation radiating from the entry points until saturation of the complete content of the nucleus is achieved. The dramatic morphological changes in the nuclei suggest a progressive disorganization of the chromatin as compound **2** accumulates, possibly due to a massive displacement of proteins bound to DNA.

Conclusions

Photophysical and DNA binding experiments have shown that novel imidazopyridinium cations **1** and **2** exhibit interesting fluorescence properties and DNA-binding ability by intercalation. Compound **2** presents the highest fluorescence quantum yield (0.32 in 5% DMSO/water and 0.46 in MeOH) and affinity for DNA (binding constant of $\sim 4.5 \times 10^5 \text{ M}^{-1}$), with a significant preference for AT-rich sequences. Moreover, the uptake and intracellular distribution of these compounds by living cells has been investigated by confocal microscopy static and time-lapse imaging. This analysis showed disruption of internal structures and a fluorescent staining compatible with apoptotic fragmentation of the nucleus for compound **1** and a clear staining pattern of interphase nuclei and metaphase chromosomes for compound **2**. The findings described here with both parent heterocycles support further studies on some representative derivatives in order to modulate the promising properties found for **1** and **2**.

Acknowledgments

Financial support from the Spanish Ministerio de Economía y Competitividad (projects CTQ2014-52488-R and CTQ2015-64425-C2-1-R), Instituto de Salud Carlos III (FEDER funds, ISCIII RETIC REDINREN RD012/20021/0014) and University of Alcalá (project CCG2015/EXP-011) is gratefully acknowledged. P. B. also thanks the University of Alcalá for his grant.

¹ (a) Xie Y, Tam VK, Tor Y. The interactions of small molecules with DNA and RNA. In: Mayer G, editor. *The chemical biology of nucleic acids*, John Wiley & Sons, Ltd, 2010, p. 115–140. (b) Hannon MJ. Supramolecular DNA recognition. *Chem Soc Rev* 2007; 36: 280–295.

² Ihmels H, Thomas L. Intercalation of organic ligands as a tool to modify the properties of DNA. In: Jin J-I, Grote J, Editors. *Materials science of DNA*, CRC Press; 2011, p. 49–75.

³ Paul A, Bhattacharya S. Chemistry and biology of DNA-binding small molecules. *Curr Sci* 2012; 102: 212–231.

⁴ Granzhan A, Ihmels H. Playing around with the size and shape of quinolizinium derivatives: versatile ligands for duplex, triplex, quadruplex and abasic site-containing DNA. *Synlett* 2016; 27: 1775–1793.

⁵ Bhadra K, Kumar GS. Therapeutic potential of nucleic acid-binding isoquinoline alkaloids: Binding aspects and implications for drug design. *Med Res Rev* 2011; 31: 821–862.

⁶ Cho MJ, Repta AJ, Cheng CC, Zee-Cheng KY, Higuchi T, Pitman IH. Solubilization and stabilization of the cytotoxic agent coralyne. *J Pharm Sci* 1975; 64: 1825–1830.

⁷ Ihmels H, Faulhaber K, Vedaldi D, Dall'Acqua F, Viola G. Intercalation of organic dye molecules into double-stranded DNA. Part 2: the annelated quinolizinium ion as a structural motif in DNA intercalators. *Photochem Photobiol* 2005; 81: 1107–1115.

⁸ Makhey D, Gatto B, Yu C, Liu A, Liu LF, LaVoie EJ. Coralyne and related compounds as mammalian topoisomerase I and topoisomerase II poisons. *Bioorg Med Chem* 1996; 4: 781–791.

⁹ Mateos E, Cebolla VL, Membrado L, Vela J, Gálvez EM, Matt M, Cossio FP. Coralyne cation, a fluorescent probe for general detection in planar chromatography. *J Chromatogr A* 2007; 1146: 251–257.

¹⁰ Sucunza D, Cuadro AM, Alvarez-Builla J, Vaquero JJ. Recent advances in the synthesis of azonia aromatic heterocycles. *J Org Chem* 2016; 81: 10126–10135.

¹¹ (a) Berdnikova DV, Aliyev TM, Paululat T, Fedorov YV, Fedorova OA, Ihmels H. DNA-Ligand interactions gained and lost: light-induced ligand redistribution in a supramolecular cascade. *Chem Commun* 2015; 51: 4906–4909. (b) Benner K, Ihmels H, Kölsch S, Pithan PM. Targeting abasic site-containing DNA with annelated quinolizinium derivatives: The influence of size, shape and substituents. *Org Biomol Chem* 2014; 12: 1725–1734. (c) Bortolozzi R, Ihmels H, Thomas L, Tian M, Viola G. 9-(4-Dimethylaminophenyl)benzo[b]quinolizinium: A near-infrared fluorophore for the multicolor analysis of proteins and nucleic acids in living cells. *Chem-Eur J* 2013; 19: 8736–8741. (d) Faulhaber K, Granzhan A, Ihmels H, Otto D, Thomas L, Wells S. Studies of the fluorescence light-up effect of amino-substituted benzo[b]quinolizinium derivatives in the presence of biomacromolecules. *Photochem Photobiol Sci* 2011; 10: 1535–1545. (e) Granzhan A, Ihmels H, Viola G. 9-Donor-substituted acridizinium salts: versatile environment-sensitive fluorophores for the detection of biomacromolecules. *J Am Chem Soc* 2007; 129: 1254–1267.

¹² (a) Norez C, Jayle C, Becq F, Vandebrouck C. Bronchorelaxation of the human bronchi by CFTR activators. *Pulm Pharmacol Ther* 2014; 27: 38–43. (b) Norez C, Bilan F, Kitzis A, Mettey Y, Becq F. Proteasome-dependent pharmacological rescue of cystic fibrosis transmembrane conductance regulator revealed by mutation of glycine 622. *J Pharmacol Exp Ther* 2008; 325: 89–99. (c) Marivingt-Mounir C, Norez C, Dérand R, Bulteau-Pignoux L, Nguyen-Huy D, Viossat B, Morgant G, Becq F, Vierfond J-M, Mettey Y. Synthesis, SAR, crystal structure, and biological evaluation of benzoquinoliziniums as activators of wild-type and mutant cystic fibrosis transmembrane conductance regulator channels. *J Med Chem* 2004; 47: 962–972.

¹³ (a) Abengozar A, Abarca B, Cuadro AM, Sucunza D, Álvarez-Builla J, Vaquero JJ. Azonia aromatic cations by ring-closing metathesis: synthesis of azaquinolizinium cations. *Eur J Org Chem* 2015; 19: 4214–4223. (b) Marcelo G, Pinto S, Cañeque T, Mariz IFA, Cuadro AM, Vaquero JJ, Martinho JMG, Maçõas EMS. Nonlinear Emission of Quinolizinium-Based Dyes with Application in Fluorescence Lifetime Imaging. *J Phys Chem A* 2015; 119: 2351–2362. (c) Abarca B, Custodio R, Cuadro AM,

- Sucunza D, Domingo A, Mendicuti F, Álvarez-Builla J, Vaquero JJ. Efficient synthesis of an indoloquinolizinium alkaloid selective DNA-binder by ring-closing metathesis. *Org Lett* 2014; 16: 3464–3467. (d) Cañeque T, Cuadro AM, Alvarez-Builla J, Pérez-Moreno J, Clays K, Castaño O, Andrés JL, Vaquero JJ. Novel charged NLO chromophores based on quinolizinium acceptor units. *Dyes Pigments* 2014; 101: 116–121. (e) Maçôas E, Marcelo G, Pinto S, Cañeque T, Cuadro AM, Vaquero JJ, Martinho JMG. A V-shaped cationic dye for nonlinear optical bioimaging. *Chem Commun* 2011; 47: 7374–7376. (f) Núñez A, Abarca B, Cuadro AM, Alvarez-Builla J, Vaquero JJ. Ring-closing metathesis approach to heteroaromatic cations: synthesis of benzo[*a*]quinolizinium salts. *Eur J Org Chem* 2011; 1280–1290. (g) Núñez A, Abarca B, Cuadro AM, Alvarez-Builla J, Vaquero JJ. Ring-closing metathesis reactions on azinium salts: straightforward access to quinolizinium cations and their dihydro derivatives. *J Org Chem* 2009; 74: 4166–4176.
- ¹⁴ (a) Granzhan A, Ihmels H, Tian M. The benzo[*b*]quinolizinium ion as a water-soluble platform for the fluorimetric detection of biologically relevant analytes. *Arkivoc* 2015; vi: 494–523. (b) Chang L, Liu C, He S, Lu Y, Zhang S, Zhao L, Zeng X. Novel styryldehydropyridocolinium derivative as turn-on fluorescent probe for DNA detection. *Sens Actuators B* 2014; 202: 483–488.
- ¹⁵ (a) Juskowiak B, Galezowska E, Koczorowska N, Hermann TW. Aggregation and G-quadruplex DNA-binding study of 6a,12a-diazadibenzo-*[a,g]*fluorenylium derivative. *Bioorg Med Chem Lett* 2004; 14: 3627–3630. (b) Feigon J, Denny WA, Leupin W, Kearns DR. Interactions of antitumor drugs with natural DNA: IH NMR study of binding mode and kinetics. *J Med Chem* 1984; 27: 450–465.
- ¹⁶ Suárez RM, Bosch P, Sucunza D, Cuadro AM, Domingo A, Mendicuti F, Vaquero JJ. Targeting DNA with small molecules: a comparative study of a library of azonia aromatic chromophores. *Org Biomol Chem* 2015; 13: 527–538.
- ¹⁷ Denny WA. Acridine-4-carboxamides and the concept of minimal DNA intercalators. In: Demeunynck M, Bailly C, Wilson WD, Editors. *Small molecule DNA and RNA binders: from synthesis to nucleic acid complexes*, Wiley-VCH; 2004, p. 482–502.
- ¹⁸ (a) Pastor J, Siro JG, García-Navío JL, Vaquero JJ, Alvarez-Builla J, Gago F, de Pascual-Teresa B, Pastor M, Rodrigo MM. Azino-fused benzimidazolium salts as DNA intercalating agents. 2. *J Org Chem* 1997; 62: 5476–5483. (b) Matia MP, García-Navío JL, Vaquero JJ, Alvarez-Builla J. Westphal condensation of *N*-aminocycloiminium salts synthesis of fused pyridazinium derivatives. *Liebigs Ann Chem* 1992; 777–779.
- ¹⁹ Prostota Y, Kachkovsky OD, Reis LV, Santos PF. New unsymmetrical squaraine dyes derived from imidazo[1,5-*a*]pyridine. *Dyes Pigments* 2013; 96: 554–562.
- ²⁰ Mendiola J, Rincón JA, Mateos C, Soriano JF, de Frutos O, Niemeier JK, Davis EM. Preparation, use, and safety of *O*-mesitylenesulfonylhydroxylamine. *Org Process Res Dev* 2009; 13: 263–267.
- ²¹ O'Connor DV, Ware WR, Andre JC. Applications of fast Fourier-transform to deconvolution in single photon-counting. *J Phys Chem* 1979; 83:1333–43.
- ²² Sybyl-X 2.0, Tripos International, 1699 South Hanley Rd., St. Louis, Missouri, 63144, USA.
- ²³ Clark M, Cramer RD III, Van Opdenbosch N. Validation of the general purpose tripos 5.2 force field. *J Comput Chem* 1989; 10, 982–1012.
- ²⁴ (a) Gallego-Yerga L, Blanco-Fernández L, Urbiola K, Carmona T, Marcelo G, Benito JM, Mendicuti F, Tros de Iarduya C, Ortiz Mellet C, García Fernández JM. Host–guest-mediated DNA templation of polycationic supramolecules for hierarchical nanocondensation and the delivery of gene material. *Chem Eur J* 2015; 21:12093–12104. (b) Carmona T, Cañeque T, Custodio R, Cuadro AM, Vaquero JJ, Mendicuti F. Cucurbit[*n*]urils as a potential fine-tuned instrument for modifying photophysical properties of D– π –A+– π –D “push–pull” chromophores. *Dyes Pigments* 2014; 103: 106–117.
- ²⁵ McConnaughie AW, Jenkins TC. Novel acridine-triazenes as prototype combilexins: synthesis, DNA binding, and biological activity. *J Med Chem* 1995; 38: 3488–501.
- ²⁶ (a) Leal JF, Martínez-Díez M, García-Hernández V, Moneo V, Domingo A, Bueren-Calabuig JA, Negri A, Gago F, Guillén-Navarro MJ, Avilés P, Cuevas C, García-Fernández LF, Galmarini CM. PM01183, a new DNA minor groove covalent binder with potent in vitro and in vivo anti-tumour activity. *Br J Pharmacol* 2010; 161: 1099–1110. (b) Leal JF, García-Hernández V, Moneo V, Domingo A, Bueren-Calabuig JA, Negri A, Gago F, Guillén-Navarro MJ, Avilés P, Cuevas C, García-Fernández LF, Galmarini CM. Molecular pharmacology and antitumor activity of Zalypsis in several human cancer cell lines. *Biochem Pharmacol* 2009; 78: 162–170. (c) Negri A, Marco E, García-Hernández V, Domingo A, Llamas-Saiz AL, Porto-Sandá S, Riguera R, Laine W, David-Cordonnier MH, Bailly C, García-Fernández LF, Vaquero JJ, Gago F. Antitumor activity, X-ray crystal structure, and DNA binding properties of thiocoraline A, a natural bisintercalating thiodipeptide. *J Med Chem* 2007; 50: 3322–3333. (d) Reddy PM, Dexter R, Bruice TC. DNA sequence recognition in the minor groove by hairpin pyrrole polyamide-Hoechst 33258 analogue conjugate. *Bioorg Med Chem Lett* 2004; 14: 3803–3807. (e)

James PL, Le Strat L, Ellervik U, Bratwall C, Nordén B, Brown T, Fox KR. Effects of a hairpin polyamide on DNA melting: comparison with distamycin and Hoechst 33258. *Biophys Chem* 2004; 111: 205–212. (f) Darby RAJ, Sollogoub M, McKeen C, Brown L, Risitano A, Brown N, Barton C, Brown T, Fox KR. High throughput measurement of duplex, triplex and quadruplex melting curves using molecular beacons and a LightCycler. *Nucleic Acids Research*. 2002; 30: e39.

²⁷ Mosmann T. Rapid colorimetric assay for cellular growth and survival: application to proliferation and cytotoxicity assays. *J Immunol Methods* 1983; 65: 55–63.

²⁸ (a) Brouwer AM. Standards for photoluminescence quantum yield measurements in solution (IUPAC Technical Report). *Pure Appl Chem* 2011; 83: 2213–2228. (b) F. Mendicuti F, Mattice WL. Suppression of the influence of stray light on quantitative measurement of I_D/I_M for weakly emitting dilute solutions of polymers. *Polym Bull* 1989; 22: 557–63.

²⁹ Lakowicz JR. Principles of fluorescence spectroscopy. 3rd ed. New York: Springer; 2006, Ch 10, p. 361.

³⁰ Lakowicz, JR. Principles of fluorescence spectroscopy. 3rd ed. New York: Springer; 2006; Ch 4, p. 97.

³¹ (a) Ardhammar M, Nordén B, Kurucsev T. DNA-drug interactions. In: Berova N, Nakanishi K, Woody RW, editors. *Circular dichroism: principles and applications*, Weinheim: Wiley-VCH; 2000, p. 741–768. (b) Johnson WC, CD of Nucleic Acids. In: Berova N, Nakanishi K, Woody RW, editors. *Circular dichroism: principles and applications*, Weinheim: Wiley-VCH; 2000, p 703–718.

³² (a) Dehkordi MN, Bordbar AK, Lincoln P, Mirkhani V. Spectroscopic study on the interaction of ct-DNA with manganese Salen complex containing triphenyl phosphonium groups. *Spectrochim Acta part A* 2012; 90: 50–54. (b) Triantafillidi K, Karidi K, Novakova O, Malina J, Garoufis A. DNA binding selectivity of oligopyridine-ruthenium(II)-lysine conjugate. *Dalton Trans* 2011; 40: 472–483. (c) Kypr J, Kejnovska I, Rencuk D, Vorlickova M. Circular dichroism and conformational polymorphism of DNA. *Nucleic Acids Res* 2009; 37: 1713–1725. (d) Karidi K, Garoufis A, Hadjiliadis N, Reedijk J. Solid-phase synthesis, characterization and DNA binding properties of the first chloro(polypyridyl)ruthenium conjugated peptide complex. *Dalton Trans* 2005; 728–734.

³³ Zhang S, Zhu Y, Tu C, Wei H, Yang Z, Lin L, Ding J, Zhang J, Guo Z. A novel cytotoxic ternary copper(II) complex of 1,10-phenanthroline and L-threonine with DNA nuclease activity. *J Inorg Biochem* 2004; 98: 2099–2106.

³⁴ (a) Tian M, Ihmels H, Ye S. Fluorimetric detection of Mg^{2+} and DNA with 9-(alkoxyphenyl)benzo[*b*]quinolinizinium derivatives. *Org Biomol Chem* 2012; 10: 3010–3018. (b) Basili S, Bergen A, Dall'Acqua F, Faccio A, Granzhan A, Ihmels H, Moro S, Viola G. Relationship between the structure and the DNA binding properties of diazoniapolycyclic duplex- and triplex-DNA binders: efficiency, selectivity, and binding mode. *Biochemistry* 2007; 46: 12721–12736. (c) Nordén B, Kurucsev T. Analysing DNA complexes by circular and linear dichroism. *J Mol Recognit* 1994; 7: 141–156.